Electrical Power and Energy Systems 113 (2019) 333–343

Contents lists available at ScienceDirect

Electrical Power and Energy Systems

journal homepage: www.elsevier.com/locate/ijepes

Cooling of overhead power lines due to the natural convection

M. Maksić[a,*], V. Djurica[a], A. Souvent[a], J. Slak[b,c], M. Depolli[b], G. Kosec[b]

[a] Elektroinstitut Milan Vidmar, Hajdrihova 2, Ljubljana, Slovenia
[b] Jožef Stefan Institute, Jamova 39 1000, Ljubljana, Slovenia
[c] Faculty of Mathematics and Physics, University of Ljubljana, Jadranska 19, Ljubljana, Slovenia

ARTICLE INFO

Keywords:
Overhead power line
Dynamic thermal rating
RBF-FD
Natural convection

ABSTRACT

The development of Dynamic Thermal Rating (DTR) systems for transmission lines in recent years has led to a better and safer utilization of the existing transmission network, as it, for most cases, enables transmission capacity of lines to be increased above the traditionally used static thermal rating value, when weather conditions are favourable. Yet, on-site measurements in the Slovenian system have also shown that many sites are regularly subject to conditions of very limited or even no winds, causing the line rating to fall well below the static value. In those conditions, the natural convective cooling can surpass forced convective cooling and correctly assessing natural convective cooling becomes crucial for the Transmission System Operators (TSO). Different mathematical models deal with natural convective cooling in different ways. Moreover, references have emerged that claim that cooling due to the natural convection gives the same results as with forced convection at 0.6 m/s crossing wind. To clarify the thermal behaviour of power lines when no external wind is present, this paper employs thermo-fluid simulation of natural convection and compares it with laboratory measurements for two different conductors. The results are also compared with CIGRE, IEEE and IEC guidelines.

1. Introduction

The opening of European-wide electricity market, the increasing penetration of intermittent renewable energy sources, and the growing power consumption have all contributed to an increasingly unpredictable power flows throughout the interconnected European transmission system. This has in many cases caused unresolved bottlenecks in parts of the system, and in worst cases also led to system-wide instabilities and blackouts, as was the case of the disturbance in 2006 [1], or the Italian blackout in 2003 [2,3]. The increased probability of system-wide instabilities has caused transmission system operators (TSOs) to re-evaluate the means of securing stable operation of the system, one of which is also the introduction of Dynamic Thermal Rating (DTR) of power lines. DTR has been introduced mainly to ensure better and safer utilization of the existing power transmission network and thus alleviate the infrastructural deficiencies, caused by the regulatory and legal issues that have virtually stopped the construction of new transmission corridors.

DTR systems calculate thermal rating, i.e. transfer capabilities of power lines based on weather measurements, such as wind, ambient temperature, solar irradiation etc. DTR models have been widely researched in the past decades [4–10]. Numerous papers deal with various phenomena affecting DTR, such as conductor heat generation and its exchange with surroundings due to radiation, solar heating, convection, and rain impinging [7]. These studies ultimately led to comprehensive guidelines provided by CIGRE [11], the IEEE [12] and the IEC [13] that were also compared in [14]. The most complex and difficult to model phenomenon within DTR is the heat exchange due to convection [15,16], forced or natural. Several widely-accepted sources [17,18], including CIGRE, IEEE and IEC guidelines, use empirical relations, pioneered by Morgan [17], to compute the power of convective cooling based on wind speed and the difference between ambient temperature and the temperature of the conductor.

In the past, line ratings were usually set to a constant value, determined by a set of unfavourable weather conditions (ambient temperature of 35 °C, low wind speed of 0.6 m/s and high solar irradiation of 800–900 W/m^2). But with the introduction of DTR, line ratings can surpass the conservative static values by a significant margin for the majority of the year. On the other hand, on-site measurements in the Slovenian system have also shown that many sites are subject to low wind speeds, which frequently fall below 0.6 m/s, causing the line ratings to fall even below the statically determined values. In low wind conditions the TSOs might thus operate their networks with overestimated thermal rating. Fig. 1 depicts the relevant wind speed

* Corresponding author.
E-mail addresses: milos.maksic@eimv.si (M. Maksić), vladimir.djurica@eimv.si (V. Djurica), andrej.souvent@eimv.si (A. Souvent), jure.slak@ijs.si (J. Slak), matjaz.depolli@ijs.si (M. Depolli), gregor.kosec@ijs.si (G. Kosec).

https://doi.org/10.1016/j.ijepes.2019.05.005
Received 23 December 2018; Received in revised form 13 March 2019; Accepted 2 May 2019

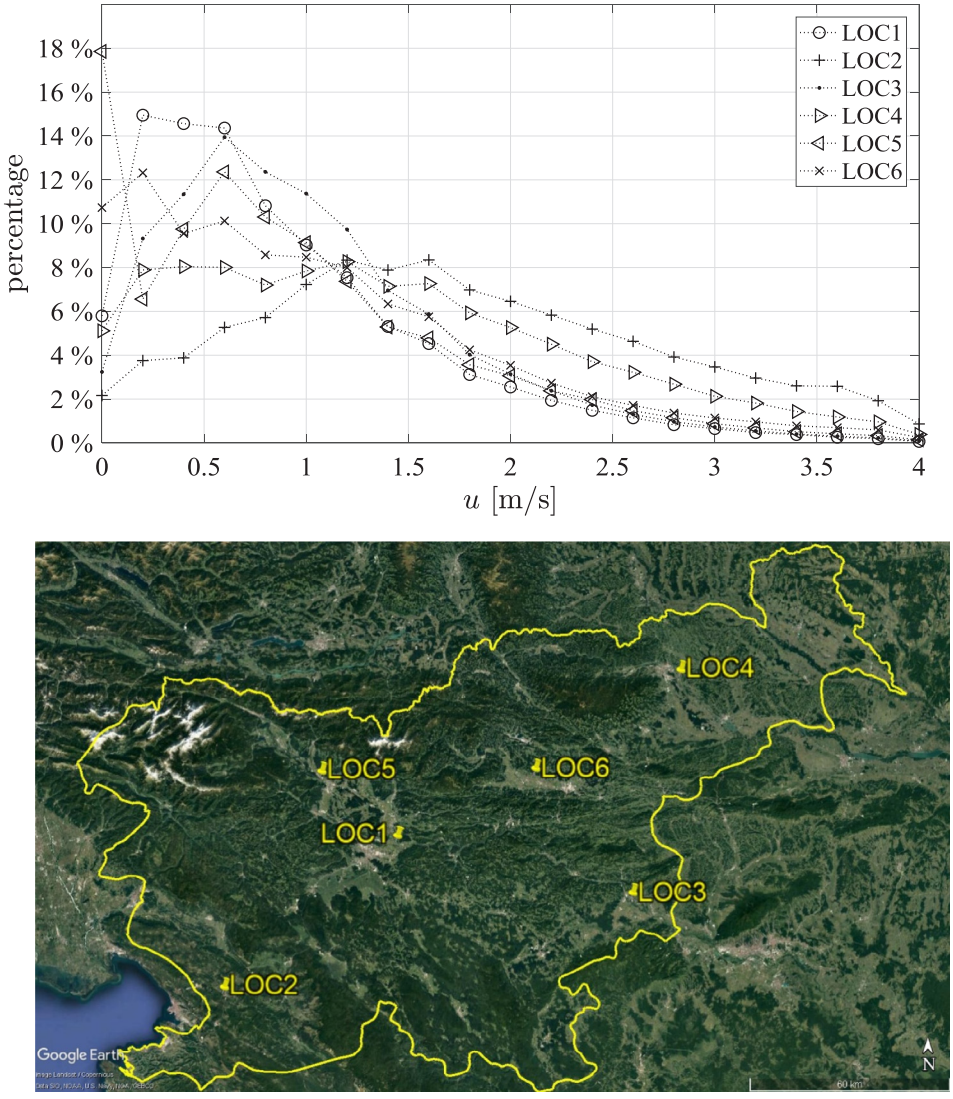

Fig. 1. Ten years of measured wind speed distributions and their 6 measurement locations in the Slovenian transmission network.

distributions over summer months on 6 locations in the Slovenian transmission system.

In case of no ($u = 0$ m/s) or very low wind speeds, which as Fig. 1 shows is a regular occurrence in Slovenia, the natural convection becomes most important cooling mechanism. DTR models of CIGRE, IEEE and IEC handle convective cooling for low wind speeds in different ways. Moreover, other references have emerged claiming that the cooling due to the natural convection gives the same results as with forced convection with a 0.6 m/s crossing wind [19]. These apparent inconsistencies need to be clarified in order to obtain a correct assessment of influence of natural convection on thermal ratings. Line thermal ratings below the static value which might occur during periods of no or very low winds can have a prevailing effect on line protection settings, net-transfer capacity (NTC) values and overall line transfer capabilities. This has motivated the Slovenian TSO to research the effects of low wind speeds on the thermal rating values.

This paper aims to clarify the thermal behaviour of power lines in regimes of no external wind, i.e. in the most unfavourable situation, by means of thermo-fluid simulation of the conductor and its immediate vicinity, laboratory measurements, and predictions offered by CIGRE, IEEE and IEC guidelines.

The rest of the paper is organized as follows. First, thermo-fluid physical model describing heat and momentum transport due to natural convection from a conductor is presented. Next, an in-house experimental setup used for measuring temperatures within and in the vicinity of the heated conductor is presented. Finally, the measurements and simulated results for two different conductor types under different conditions are presented. Based on the results, the conclusions of the paper are summarized.

2. Simulation of convective cooling

CIGRE, IEEE and IEC guidelines for computing the convective cooling rely on empirical relations. IEEE and CIGRE differentiate between low wind and high wind regimes, and treat the natural convection as a special regime, while IEC does not consider natural convection as a special regime.

In all three cases, the cooling power (P_C) of natural convection is modelled as

$$P_C = \pi (T_s - T_a) \lambda Nu \left[\frac{\mathrm{W}}{\mathrm{m}}\right] \tag{1}$$

where T_s [°C] stands for the skin temperature of the conductor, T_a [°C] for ambient temperature, Nu for Nusselt number and λ [W/mK] for thermal conductivity of air. In CIGRE, Nusselt number is modelled as

$$\mathrm{Nu} = \xi \left(\frac{\rho^2 c_p g \beta (T_s - T_a) D^3}{\lambda \mu} \right)^m, \tag{2}$$

where ξ and m are empirically obtained dimensionless parameters, and λ [W/mK], c_p [J/kg K], ρ [kg/m^3], β_T [K^{-1}], μ [kg stand for air /ms], D [m] *and* $\boldsymbol{g}$ [m/s^2]
thermal conductivity, air specific heat, air density, air thermal expansion coefficient, air viscosity, line diameter and gravitational acceleration, respectively.

IEEE employs a similar approach and models P_C as

$$P_C = 3.645\rho^{0.5}D^{0.75}(T_s - T_a)^{1.25}\left[\frac{\mathrm{W}}{\mathrm{m}}\right]. \tag{3}$$

IEC does not treat natural convection as a special regime and the relation (1) for forced convection is used also in zero wind situations, where the Nusselt and Reynold numbers are computed as

$$Nu = 0.65\,Re^{0.2} + 0.23Re^{0.6}, \tag{4}$$

$$Re = 1.644{\cdot}10^9 uD\left(\frac{T_a + T_s}{2}\right)^{-1.78}, \tag{5}$$

resulting in zero convective cooling in the absence of forced convection ($u = 0$ m/s). All the details about the discussed models can be found in CIGRE [11], IEEE [12] and IEC [13] brochures.

In this paper we present a model that estimates conductor temperature by means of thermo-fluid simulation in the vicinity of the power line instead of relying on empirical relations, as it is done in CIGRE, IEEE and IEC. The domain of the simulation is represented as a square of air around the power line, and the power line itself, which is further separated into ACSR (Aluminium Conductor Steel Reinforced) conductor. In the steel core, only heat conduction takes place, governed by

$$c_p^{st}\rho^{st}\frac{\partial T^{st}}{\partial t} = \lambda^{st}\nabla^2 T^{st}, \tag{6}$$

while in the aluminium part, heat generation due to Joule losses is also present, described by

$$c_p^{al}\rho^{al}\frac{\partial T^{al}}{\partial t} = \lambda^{al}\nabla^2 T^{al} + q_J, \tag{7}$$

where indices *st* and *al* denote steel and aluminium domains, c_p [J/kgK] specific heat capacity, λ [W/mK] radial thermal conductivity, ρ [kg/m^3] density, T [°C] temperature, and $q_j\,[W/m^2]$ heat source due to the Joule losses, which is modelled as

$$q_j = \frac{I^2R(T)}{S^{al}}. \tag{8}$$

Here, $I\,[A]$ stands for electric current, S^{al} [m^2] is the cross-section area of the conductor and the temperature dependent resistance $R(T)$ [Ω] is introduced as [11]

$$R(T) = R_{20}(1 + \alpha_{20}(T - 20°\mathrm{C})), \tag{9}$$

where R_{20} stands for resistivity at 20 °C and $\alpha_{20}\,[K^{-1}]$ is the thermal resistance coefficient at 20 °C. The power line is surrounded by air (a fluid), which demands that momentum transport is to be considered in addition to the heat transport. The thermo-fluid transport in the air is modelled by Navier-Stokes equation and mass continuity is further coupled with the heat transfer through the Boussinesq approximation

$$\nabla{\cdot}\boldsymbol{v} = 0, \tag{10}$$

$$\rho\frac{\partial \boldsymbol{v}}{\partial t} + \rho\nabla{\cdot}(\boldsymbol{v}\boldsymbol{v}) = -\nabla P + \nabla{\cdot}(\mu\nabla\boldsymbol{v}) + \boldsymbol{b}, \tag{11}$$

$$\rho\frac{\partial(c_pT)}{\partial t} + \rho\nabla{\cdot}(c_pT\boldsymbol{v}) = \nabla{\cdot}(\lambda\nabla T), \tag{12}$$

$$\boldsymbol{b} = \rho[1 - \beta(T - T_{\mathrm{ref}})]\boldsymbol{g}. \tag{13}$$

$\boldsymbol{v} = (u, v)[m/s]$, $P[Pa]$, T [°C], $\lambda\,[W/mK]$, $c_p[J/kgK]$, $\boldsymbol{g}\,[m/s^2]$, and $\rho\,[kg/m^3]$, $\beta\,[K^{-1}]$, T [°C], $\mu\,[kg/ms]$
$\boldsymbol{b}\,[kg/m^2s^2]$ stand for air velocity, air pressure, air temperature, air thermal conductivity, air specific heat, gravitational acceleration, air density, the coefficient of thermal expansion of air, reference temperature for Boussinesq approximation, air viscosity and body force, respectively. Thermal conductivity and viscosity of air are further modelled as [11]

$$\lambda = 2.368{\cdot}10^{-2} + 7.23{\cdot}10^{-5}T - 2.763{\cdot}10^{-8}T^2\left[\frac{\mathrm{W}}{\mathrm{mK}}\right], \tag{14}$$

$$\mu = (17.239 + 4.635{\cdot}10^{-2}T - 2.03{\cdot}10^{-5}T^2){\cdot}10^{-6}\left[\frac{\mathrm{kg}}{\mathrm{ms}}\right]. \tag{15}$$

To close the above system, an appropriate set of boundary conditions is required. On the boundary between the ACSR and surrounding air

$$T^{al}(r_1) = T^{st}(r_1), \tag{16}$$

$$\lambda^{al}\frac{\partial T^{al}}{\partial \boldsymbol{n}}\bigg|_{r_1} = \lambda^{st}\frac{\partial T^{st}}{\partial \boldsymbol{n}}\bigg|_{r_1}, \tag{17}$$

$$T^{al}(r_2) = T(r_2), \tag{18}$$

$$\lambda^{al}\frac{\partial T^{al}}{\partial \boldsymbol{n}}\bigg|_{r_2} - \lambda\frac{\partial T}{\partial \boldsymbol{n}}\bigg|_{r_2} = q_r, \tag{19}$$

holds, where r_1 [m] and r_2 [m] denote the radii of the steel core and the power line, respectively, $\mathbf{n}$ denotes the outside unit normal vector to the domain boundary, and q_r [W/m] heat sink due to radiation, modelled as

$$q_r = -\sigma_B\varepsilon_s(T_s^4 - T_a^4), \tag{20}$$

with $\sigma_B = 5,67$ W/m^{2}K^4 and ε_s standing for the Stefan-Boltzmann constant and emissivity, respectively. At the top boundary, symmetry is assumed, yielding conditions

$$\frac{\partial \boldsymbol{v}}{\partial y}\bigg|_{top} = 0, \tag{21}$$

$$\frac{\partial T}{\partial y}\bigg|_{top} = 0. \tag{22}$$

Other two boundaries are assumed to be far enough away that air is still and at ambient temperature.

The presented model is solved with explicit Euler time discretization scheme. Mass continuity is enforced by solving pressure correction Poisson's equation, and the spatial discretization is done with a meshless method. The core of the meshless numerical method is an approximation of the considered field and its derivatives on overlapping support domains. For each discretization node, an approximation of the field over a local support domain is constructed. This approximation is then used to compute the so-called shape functions which are used to compute the approximations of field derivatives. Shape functions can be computed with different approaches, e.g. least squares, collocation, augmented collocation, etc. The strongest advantage of the presented method is that all the building blocks are independent of each other and can be therefore elegantly coded as abstract modules, not knowing about each other in the core of their implementation. Such approach offers great flexibility in the implementation of different features that are planned for the future, e.g. hyperviscosity or adaptive upwind to treat convection dominated transport, adaptivity to better capture behaviour near the conductor, generalisation to 3D and potentially more complex models. The numerical solution procedure of problem at hand uses with a well-researched RBF-FD [20] variant of meshless methods implemented by an in-house meshless Medusa library [21].

The numerical solution of the presented model for Al/Fe 490/65 conductor (refer to section Experimental setup for details) is demonstrated in Fig. 2 in terms of temperature and velocity magnitude contour plots for various differences between ambient and skin temperature ($\Delta T = T_s - T_a$).

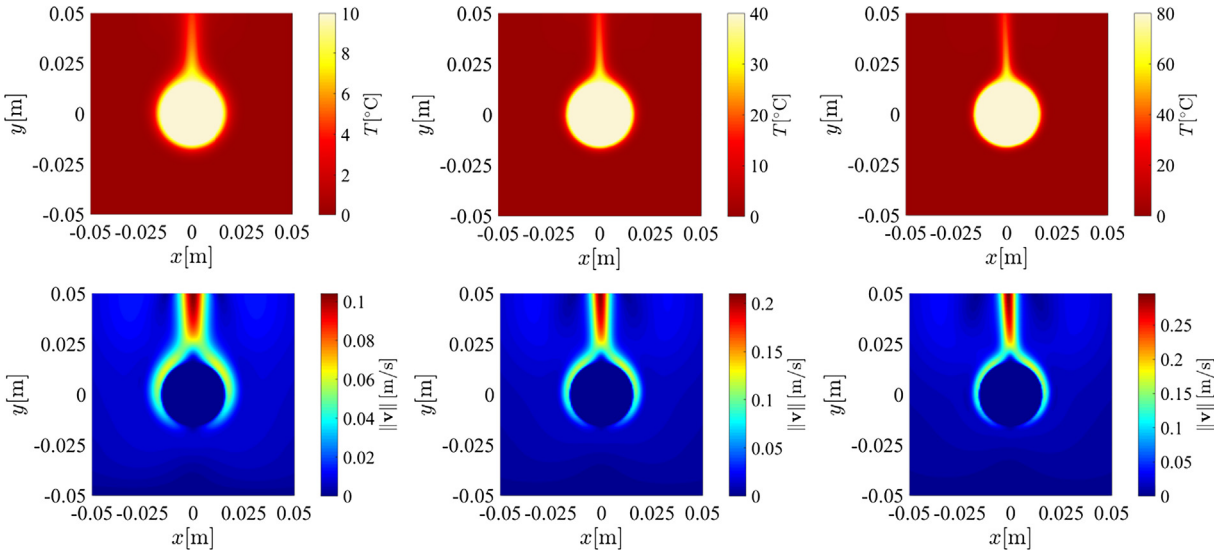

Fig. 2. Simulated temperature and velocity magnitude contour plots for $\Delta T = 10$ °C (left column), $\Delta T = 40$ °C (middle column) and $\Delta T = 80$ °C (right column).

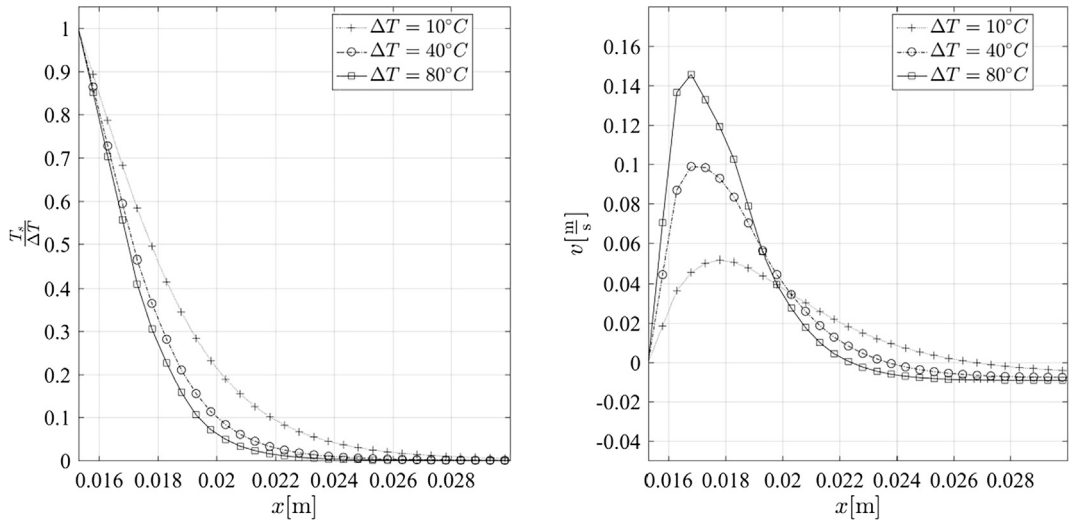

Fig. 3. Temperature cross section $T(x, y = 0)$ (left) and vertical velocity component $v(x, y = 0)$ (right) at ambient–skin temperature differences ΔT.

As expected, a jet of warm air forms above the power line. By increasing the temperature difference between the air and the skin, the jet intensifies and narrows, which can be seen in Fig. 3, where temperature and velocity cross-section profiles are presented.

It can also be seen from Fig. 3 that the thickness of the boundary layer is in the order of few centimetres, much less than the dimension of the computational domain. In left part of Fig. 4, convergence with respect to the spatial and temporal discretization step is presented. In the right part of Fig. 4 the response of simulation to the perturbation of thermo-physical properties of air is shown. The solution converges at roughly $N = 10^5$ nodes and, as expected, becomes unstable for such nodal density at time step of approximately $\Delta t = 10^{-3}$, due to the explicit treatment. Based on these observations, a 0.1 m × 0.1 m domain, discretized with $N = 10^5$ nodes, is used in all following simulations with explicit time stepping with $\Delta t = 10^{-4}$.

In Fig. 5 a comparison of natural convection assessments between the simulation and the IEEE, CIGRE, and IEC models is presented. While IEC assumes no heat transfer from the power line to the surroundings and hence completely fails to predict this regime, CIGRE and IEEE models behave similarly to the simulation. Due to the high agreement between CIGRE and IEEE computations only one will be presented in all future analyses, namely CIGRE.

3. Experimental setup

In order to replicate the behaviour of overhead lines in conditions with no wind ($u = 0$ m/s), when only natural convection is present, a closed indoor laboratory experiment was set up (Fig. 6).

A conductor is connected to a laboratory class 0.1% precision current transformer with 2500 A:5 A ratio and forms a closed current loop, operating at low voltage. The AC current output of the current transformer is determined with a regulation transformer which is in turn set with a hybrid DTR controller. Conductor and ambient temperature measurements are sampled and sent to the controller, which can either hold the current constant or can control the line temperature to a constant value. The controller controls the servo mechanisms of the variable transformer. This affects the voltage on the transformer's secondary side and thus also the current that is flowing through the conductor current loop. In our measurements the current in the loop is held constant, since the line is not exposed to outdoor conditions and therefore there are no external factors (e.g. wind, solar irradiation) which can affect the line temperature. An IT system stores all the measurements and the data related to the operation of the controller in a database and enables remote visualization and control of the system.

Two power conductors have been tested, namely a weathered 243-

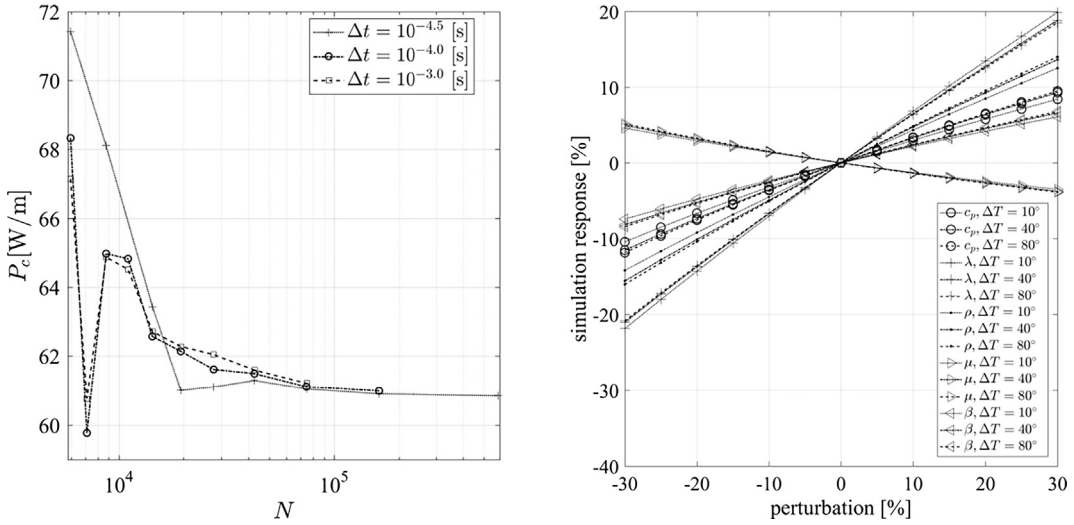

Fig. 4. Convergence (left) and stability regarding the thermo-physical properties (right) of the simulation.

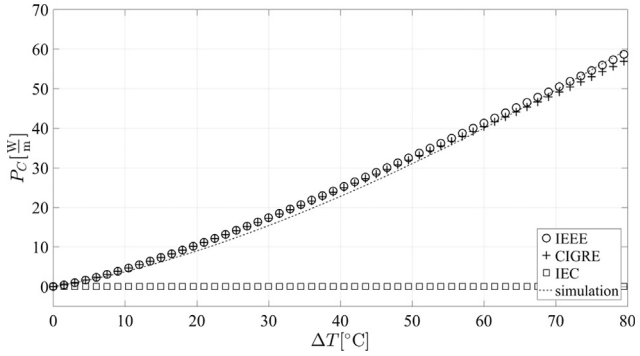

Fig. 5. Cooling power of natural convection with respect to ΔT computed by IEEE, CIGRE, IEC and simulation.

AL1/39-ST1A also referred to as Al/Fe 240/40 and a brand new 490-AL1/64-ST1A also referred to as Al/Fe 490/65, in the form of current loops. Their material properties are shown in Table 1, while the different specifications of both conductors are in Table 2. Measurements during the factory acceptance tests have determined that the parameters of both conductors are the same as listed in EN 50182 standard. As per CIGRE guidelines [11], emissivity of conductors increases with age from about 0.2–0.3 for new conductors to 0.8–0.9 when exposed to weathering. Based on these guidelines we assumed emissivity 0.25 for a brand new 490-AL1/64-ST1A conductor and emissivity 0.85 for a weathered 243-AL1/39-ST1A conductor.

Two closed conductor loops shown in Fig. 7 are suspended at a height of approximately 1.5 m above ground and are positioned well clear of any obstacles that might obstruct the convective flow of air around them. The length of the conductors is 6 m and the two outer conductors are separated by 2 m. The conductors are placed on insulators which enable galvanic separation from the rest of the measurement apparatus. Sensors are placed on one of the two outer conductors (either 240 mm^2 or 490 mm^2, depending on the measurements performed) which are connected with copper busbars to the two 490 mm^2 inner conductors. These serve only as a current return path and play no active role in the experiment itself. Although the return paths are also heated by Joule losses, it can be seen from Fig. 2 that the boundary layer of the natural convection is in the order of a few centimetres, while the conductors are 40 cm apart. Therefore we can safely assume that the natural convection induced by return paths does not interfere with the experiment. The whole experiment is mounted on wheels and can be moved anywhere in the laboratory, but is stationary when the measurements are running. A side view of the setup is shown in Fig. 8.

There are 16 line and ambient temperature sensors positioned around the apparatus. The line sensors measure the temperature either on the surface or in the core of the line and are designated as TC (thermocouple) sensors. TC sensors must be sufficiently small in order to be precisely inserted into the aluminium strands of the line, as shown on left side in Fig. 9. For this reason, a thermocouple (TC) of 0.2 mm size was chosen. The next group are cold junction (CJ) sensors which measure ambient temperature (shown in the middle of Fig. 9). All sensors are calibrated within ± 0.5 °C accuracy in the range of –40 °C to 125 °C. Special care was devoted to the placement of the sensors and wires connected to the sensors and measuring devices, so that they do not interfere with the experiment and cause turbulences in the flow of heated air flowing around the conductor. This was avoided by introducing a small spacing between the sensors (Fig. 9, right).

Finally, the positioning of TC sensors on the surface and in the core of the conductor is shown in Fig. 10. Eight additional sensors on the surface are placed horizontally, about 40 cm apart.

The temperature measurement range of the sensors ranges from –20 to 85 °C. The measurement error of all sensors is ± 1 °C.

The thermocouple voltage is converted with AD conversion to a proper temperature reading. Additionally, the compensation of cold-junction temperature and the linearization of the signal are performed. A proper conduction of heat and good electrical conductivity between the sensors and the wire is achieved with a contact of the thermocouple to the line. Due to the AC current flowing through the line, the TC sensors are on a sinusoidal 50 Hz potential with all the accompanying harmonics. As the measuring converter is on a fixed electrical potential and the sensors are on a floating potential, we used an isolation SPI (Serial to Peripheral Interface) and I^2C (Inter-Integrated Circuit) bus for the conversion, which eliminates any possible effects of the difference of electrical potentials.

To give an example of the extent of deviations of measured temperatures, Fig. 11 shows the difference in temperatures measured with sensors TC0 and TC3, which are placed symmetrically on the surface of conductor Al/Fe 490/65 as in Fig. 10, for the period of approximately 13 h. The deviations do not surpass 1 °C. Additionally, the plot on the right of Fig. 11 shows that there is little correlation between the temperature deviations and the average conductor temperature.

4. Comparison of simulation, CIGRE and measurements

Conductor temperatures measured in the closed laboratory setup

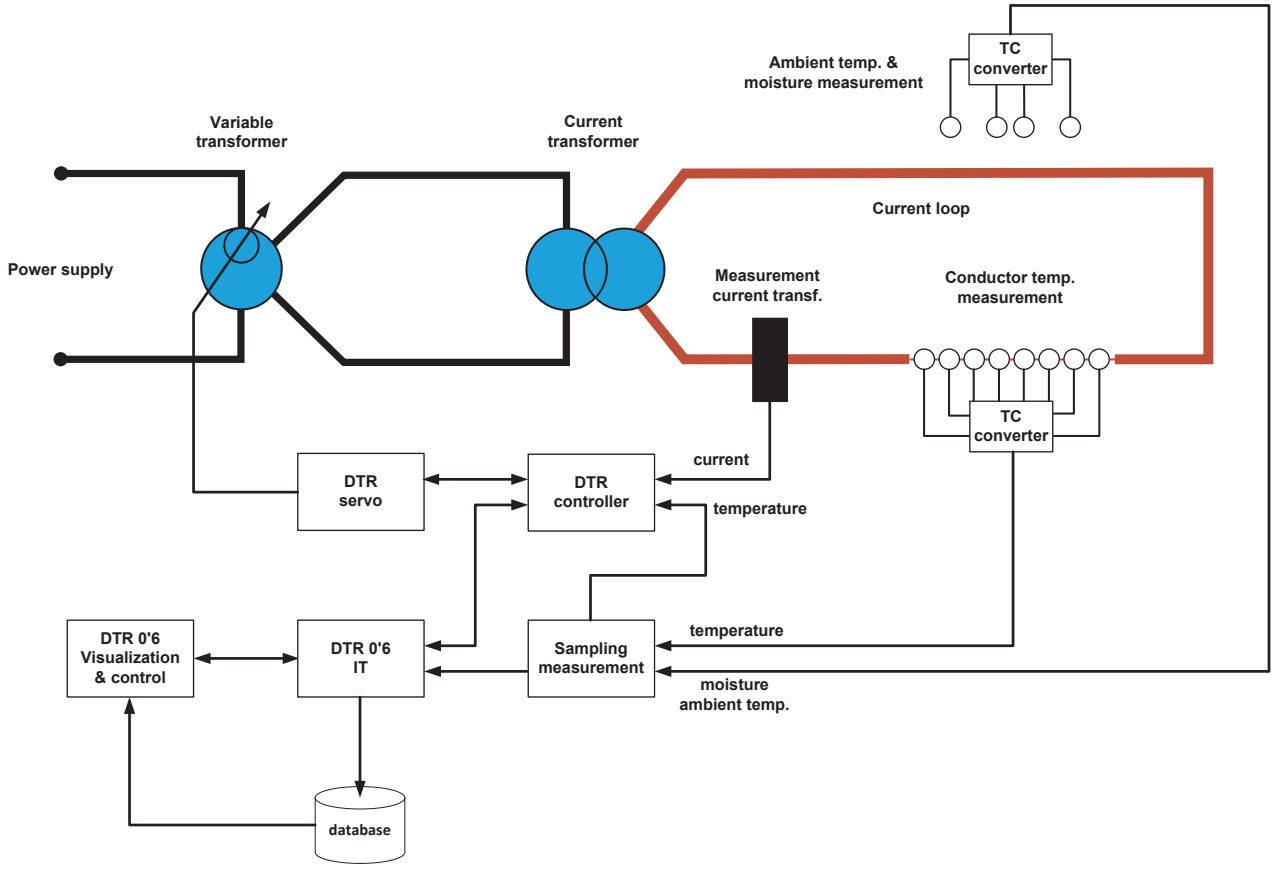

Fig. 6. Scheme of the experiment.

Table 1
Material properties of conductors.

Parameter		Value
Steel density	$\rho_{St}\,[kg/m^3]$	7780
Aluminium density	$\rho_{Al}\,[kg/m^3]$	2703
Specific heat of aluminium	c_{pAl} [J/kgK]	897
Specific heat of steel	c_{pSt} [J/kgK]	481
Electrical conductivity of aluminium	$S_{al}\,[1/(m\Omega)]$	$35{\cdot}10^6$
Electrical conductivity of steel	$S_{St}\,[1/(m\Omega)]$	$1.45{\cdot}10^6$
Thermal resistance coefficient of aluminium	$\alpha_{al}\,[1/K]$	$4.03{\cdot}10^{-3}$

Table 2
Specifications of two conductors used in measurements.

		243-AL1/39-ST1A	490-AL1/64-ST1A
Steel part radius	$r_1\,[m]$	0.004	0.005
Conductor radius	$r_2\,[m]$	0.0109	0.0153
Radial thermal conductivity	$\lambda_{Al,St}$ [W/mK]	4.0	2.0
Emissivity	ε	0.85	0.25

are presented next and compared with the results obtained through simulation. Several different experiments with conductors Al/Fe 240/40 and Al/Fe 490/65 were performed. Each experiment was defined as follows. In the initial state, the whole conductor is at the ambient temperature, equal to the room temperature of the laboratory. The step change in the current flowing through the conductor is then performed which causes a gradual increase of the conductor temperature. Once the temperature settles to a steady state, the current is once again increased, which causes further rise in the conductor temperature. This sequence is repeated several times for each measurement, whereas the chosen step increase in current and the wait time for the temperature to settle depend on the conductor type. At the end of each experiment, the current is turned off and the conductor is left to cool down to the ambient temperature.

Altogether four measurements for Al/Fe 490/65 and two for Al/Fe 240/40 were performed. This was enough to scan the entire temperature range that is relevant for thermal rating for both conductors. For Al/Fe 240/40, the current ranged from 50 to 700 A and the conductor core temperature reached between 25 °C and 80 °C. The current range for Al/Fe 490/65 was between 300 and 1000 A, and the core temperature reached between 35 °C and 95 °C. Measurements were carried out in early spring (a total 26.3 h of measurements on Al/Fe 490/65 in March), in the summer (24.9 h of measurements on Al/Fe 490/65 in August) and in the autumn (13 h of measurements on Al/Fe 490/65 and 28.9 h of measurements on Al/Fe 240/40 in September and October), all in 2018.

Two sets of measurements for Al/Fe 490/65 are presented in Fig. 12 and two sets for Al/Fe 240/40 in Fig. 13. Measured surface (skin) temperature of conductors is compared with the computed temperatures, obtained by the simulator described in chapter 2, and to the published CIGRE guidelines. T_s^M represents the average temperature of all measurements on the conductor surface in Fig. 10. The red line in Fig. 12 and 13 denotes the current flowing through the conductor, T_s^S is the surface temperature obtained with the simulator, T_s^C is the surface temperature obtained with CIGRE equations, T_S^M is the average measured surface temperature and T_a the ambient temperature. Ambient temperature was relatively constant throughout the measured period. There was no solar irradiation heating of the conductor and no external wind. Between the successive step changes, the current is not entirely constant due to the heating of the conductor increasing its resistance, and due to the inability of the used variable transformer to stay on

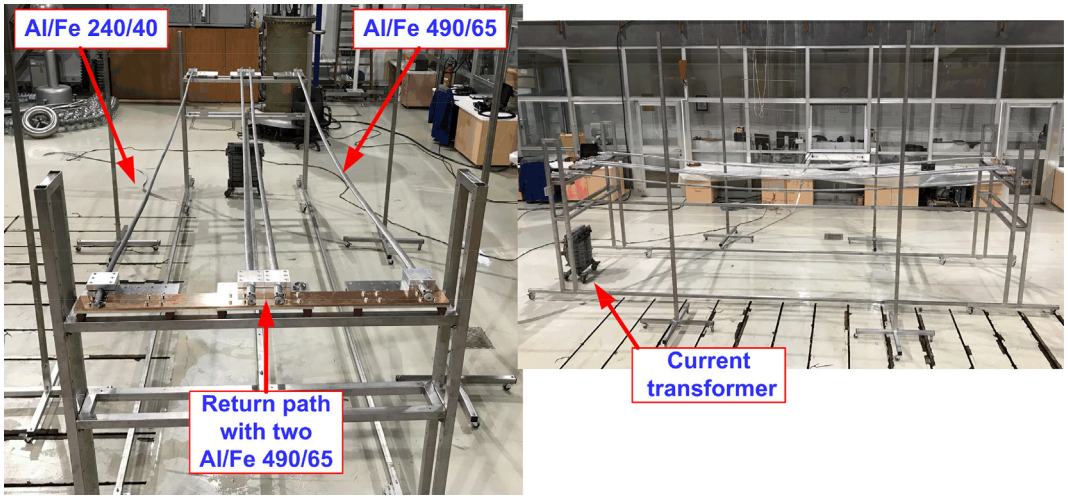

Fig. 7. Experimental setup with mounted conductors.

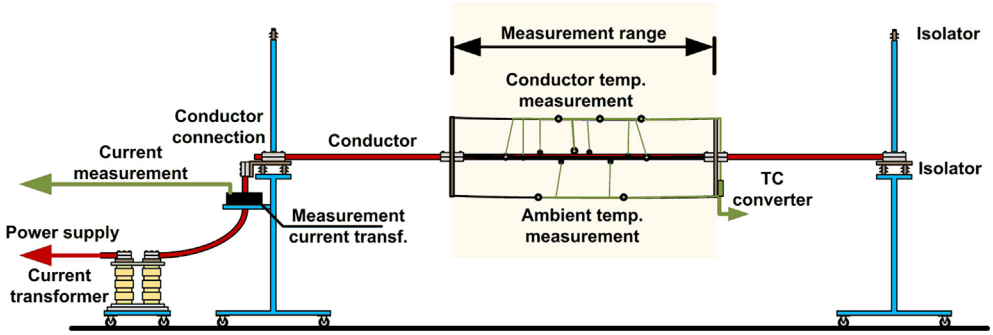

Fig. 8. Side view of the experimental setup.

exactly the desired tap.

On the left-hand side of Fig. 12, we can observe that the conductor temperature, changed by the step increase in current, settled in approximately 4 h. There is relatively good agreement between measured and simulated, with both the simulator and CIGRE equations, temperatures, with the error mostly below 3%. The noticeable difference between computed results and measurement data is in the final cooling temporal development. Both computational approaches, however, provide similar result, which implies that the underlying reason could be in provided thermo-physical properties of the conductor, namely density and specific heat that have to be appropriately accounted for due to strand packing [22]. A more precise study of this phenomenon will be carried out in our future measurements.

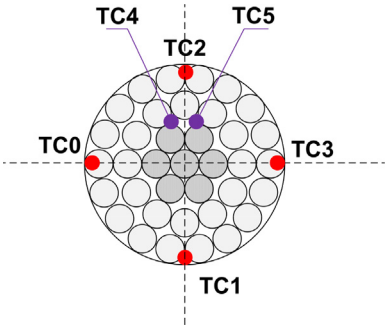

Fig. 10. Cross section of conductor with placement of TC sensors.

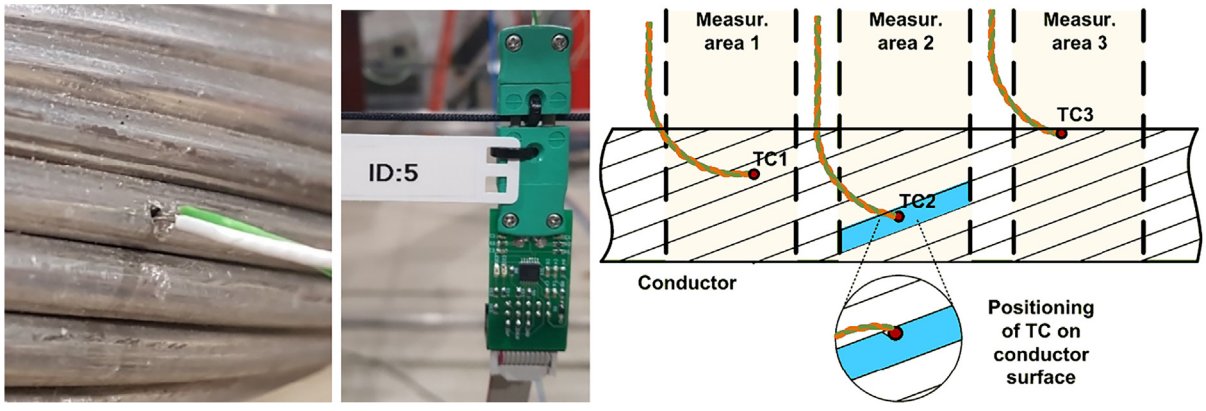

Fig. 9. Surface temperature measurement TC (left), ambient temperature measurement CJ (middle), placement of sensors (right).

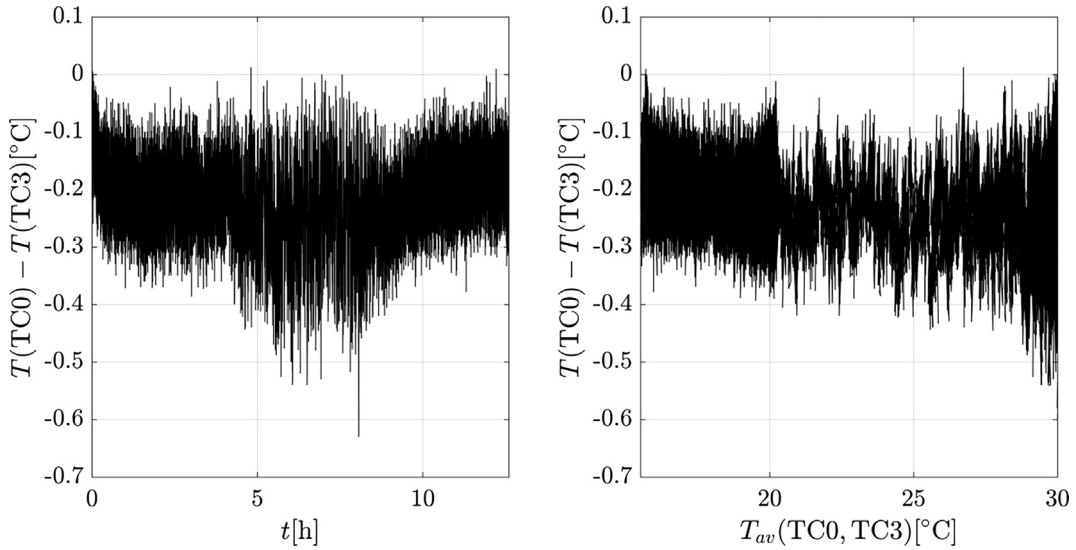

Fig. 11. Deviations of temperatures measured on the conductor surface with sensors TC0 and TC3 with respect to time (left) and the average conductor temperature (right).

For the conductor Al/Fe 240/40 the comparison of measured and computed results is presented in Fig. 13. Due to the smaller mass of this conductor relative to the Al/Fe 490/65, the time for the temperatures to settle is decreased and the intervals between successive current steps are also shorter, about 2.5 h. The differences between measured and computed temperatures are about 2% in this case.

Measured and computed steady state temperatures along with relative difference between surface temperatures obtained by measurements (T_s^M [°C]), simulation (T_s^S[°C]), and CIGRE (T_s^C[°C]), are shown in Table 3 and Fig. 14 for Al/Fe 240/40 and in Table 4 and Fig. 15 for Al/Fe 490/65.

Note that each data point in the figure effectively represents one measurement, or more precisely, one steady-state situation. For example, 3 × 8 data points in Fig. 14 are from 8 steady-state measurements on Al/Fe 240/40 shown in Fig. 13, where the relative difference between simulated and measured temperatures is denoted with circles, the relative difference between temperatures computed with CIGRE and measured temperatures with crosses, and relative difference between simulated and computed temperatures with CIGRE with squares. The bottom plots of Fig. 15 and Fig. 14 show the ambient temperature and current for these cases. For temperatures below 50 °C, the resulting relative differences for both CIGRE and simulator are generally negative, meaning that calculated temperatures were smaller than measured ones. But the differences are small, i.e. absolute value does not surpass 2%. For surface temperatures greater than 50 °C these differences are even smaller, i.e. absolute value does not surpass 1%. Third set of points (squares) show the relative difference of temperatures obtained by simulation and CIGRE. Methods are in good agreement and the absolute value of errors does not surpass 1% value.

Similar plots as in Fig. 14 are shown in Fig. 15 for Al/Fe 490/65. For this conductor the relative errors are larger, but rarely surpass 3% value. Unlike the previous conductor, this time the calculated temperatures are generally larger than measurements. Again, both computational methods provide approximately the same results with the errors below 2%. Larger errors compared to Al/Fe 240/40 could be accounted to the larger span of ambient temperatures in the laboratory – T_a spanned from 10 °C to 30 °C (bottom of Fig. 14), compared to only 1 °C difference of T_a for Al/Fe 240/40 in Fig. 15. More measurements, especially for Al/Fe 240/40, will be performed in future to thoroughly examine the effect of ambient temperature.

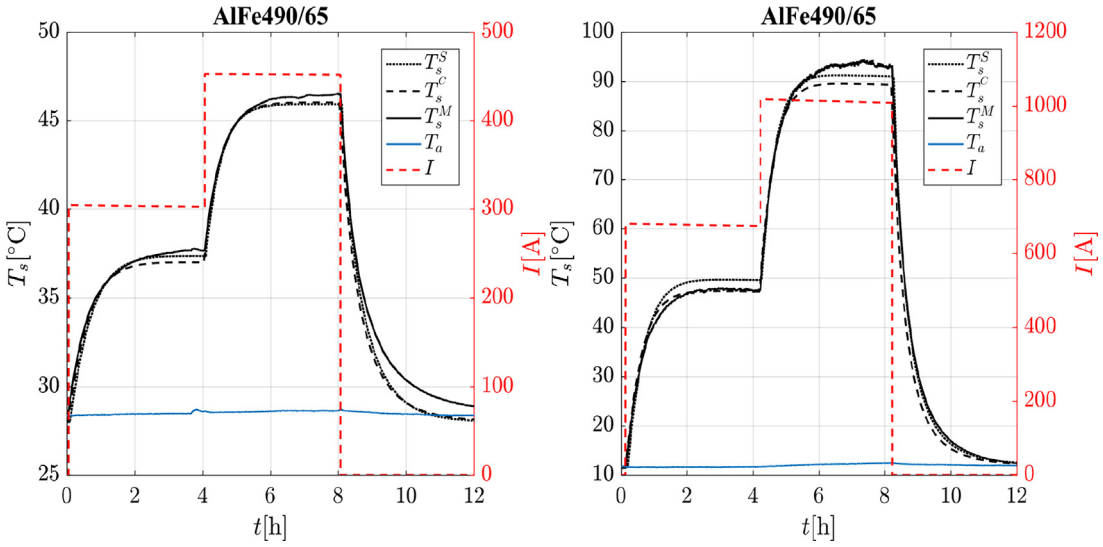

Fig. 12. Temporal development of temperature on skin of Al/Fe 490/65 during measurement.

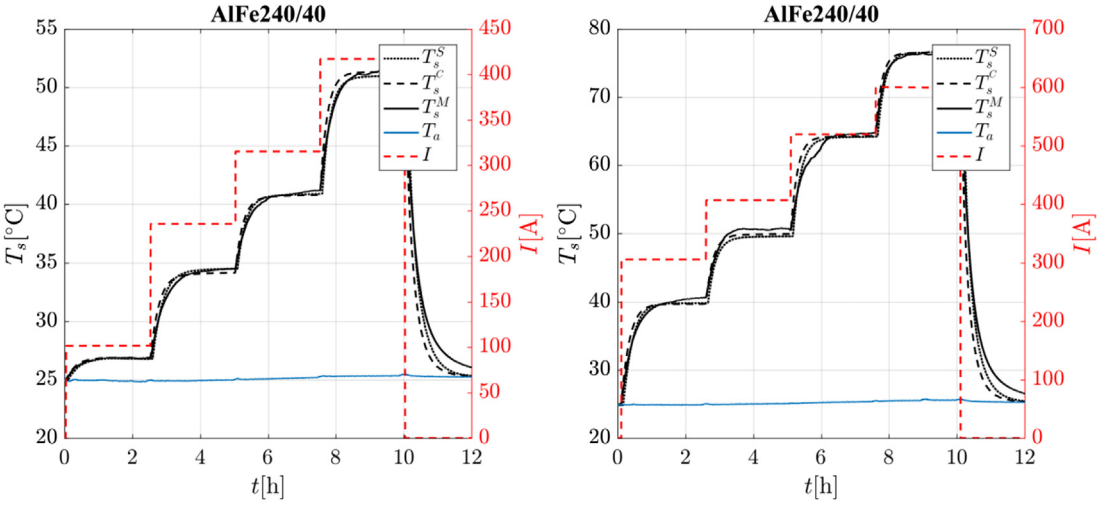

Fig. 13. Temporal development of temperature on skin of Al/Fe 240/40 during measurement.

Table 3
Measured and calculated steady state temperatures with relative differences for Al/Fe 240/40.

Al/Fe 240/40	T_s^M [°C]	T_s^S [°C]	T_s^C [°C]	$\frac{T_s^S - T_s^M}{T_s^M}$	$\frac{T_s^C - T_s^M}{T_s^M}$	$\frac{T_s^S - T_s^C}{T_s^M}$
Measurement 1	26.9	26.8	26.8	–0.0031	–0.0025	–0.0007
Measurement 2	34.4	34.5	34.1	0.0023	–0.0075	0.0097
Measurement 3	40.3	39.8	39.7	–0.0126	–0.0157	0.0031
Measurement 4	41.0	40.8	40.8	–0.0027	0.0047	0.0020
Measurement 5	50.5	49.6	49.9	–0.0189	–0.0120	0.0069
Measurement 6	51.1	50.9	51.3	–0.0035	0.0037	–0.0072
Measurement 7	64.6	64.2	64.3	–0.0061	–0.0041	–0.0020
Measurement 8	76.3	76.5	76.5	0.0023	0.0022	0.0001

Table 4
Measured and calculated steady state temperatures with relative differences for Al/Fe 490/65.

Al/Fe 490/65	T_s^M [°C]	T_s^S [°C]	T_s^C [°C]	$\frac{T_s^S - T_s^M}{T_s^M}$	$\frac{T_s^C - T_s^M}{T_s^M}$	$\frac{T_s^S - T_s^C}{T_s^M}$
Measurement 1	19.8	20.0	20.1	0.0124	0.0142	–0.0018
Measurement 2	29.4	30.0	30.1	0.0224	0.0263	–0.0040
Measurement 3	37.3	37.2	36.9	–0.0001	–0.0089	0.0088
Measurement 4	46.3	45.9	46.0	–0.0084	–0.0064	–0.0019
Measurement 5	56.0	57.2	57.3	0.0216	0.0238	–0.0022
Measurement 6	72.6	73.1	74.2	0.0069	0.0213	–0.0144
Measurement 7	72.6	73.0	74.0	0.0047	0.0190	–0.0142
Measurement 8	93.1	91.2	89.5	–0.0201	–0.0383	0.0182

5. Discussion

With analyses presented so far we have established confidence in computationally obtained conductor temperature. With a validated solution procedure we verify a claim that minimal equivalent wind velocity never drops below 0.6 m/s, i.e. that power line is always cooled as if there were at least 0.6 m/s ambient wind [19]. The claim is based either on the fact that there is always at least 0.6 m/s of ambient wind in nature, as assumed in [23], or that sole natural convection provides such cooling power. In the beginning of the paper it was demonstrated that in the last 10 years the measured wind speed was below 0.6 m/s for a significant portion of time, therefore the first assumption is refuted. To verify the second assumption, the EN 50182 standard [24] is examined. According to [24], in nominal operating conditions (wind velocity of 0.6 m/s with 90° angle, ambient temperature of 35 °C and solar irradiation of 900 W/m^2), the conductor Al/Fe 240/40 reaches temperature of 80 °C at a current of 640 A, and Al/Fe 490/65 reaches the same temperature at 960 A. Simulation at no wind and with only natural convection predicts that Al/Fe 240/40 conductor reaches temperature of 107 °C at 640 A and Al/Fe 490/65 also reaches 107 °C at 960 A, which is in stark contrast to the EN 50182 standard. Even with no solar irradiation, the temperature of Al/Fe 490/65 is well above

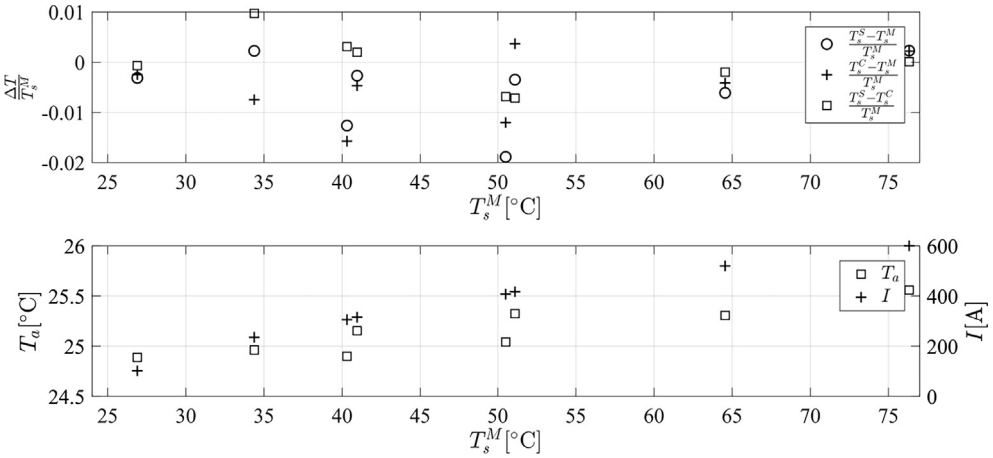

Fig. 14. Relative difference between measurements and model prediction in steady state skin temperature (top) at different conditions (bottom) for Al/Fe 240/40 conductor as a function of measured skin temperature.

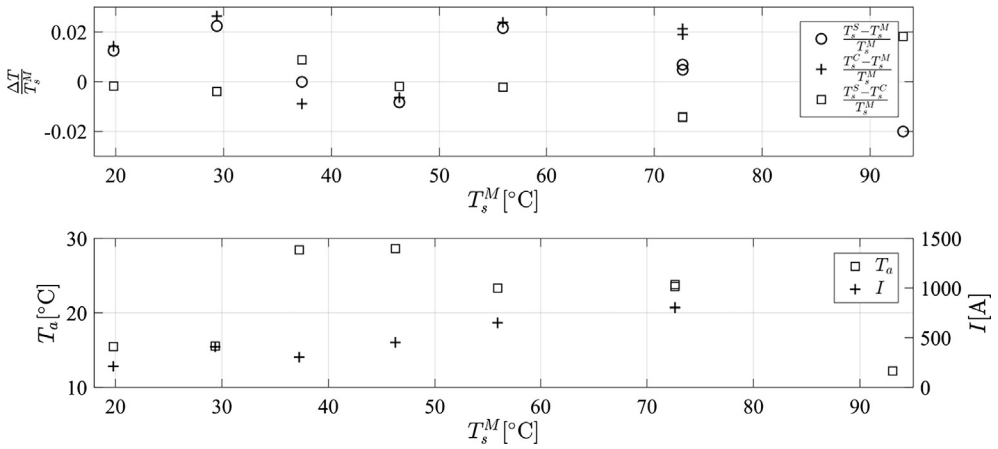

Fig. 15. Relative difference between measurements and model prediction in steady state skin temperature (top) at different conditions (bottom) for Al/Fe 490/65 conductor as a function of measured skin temperature.

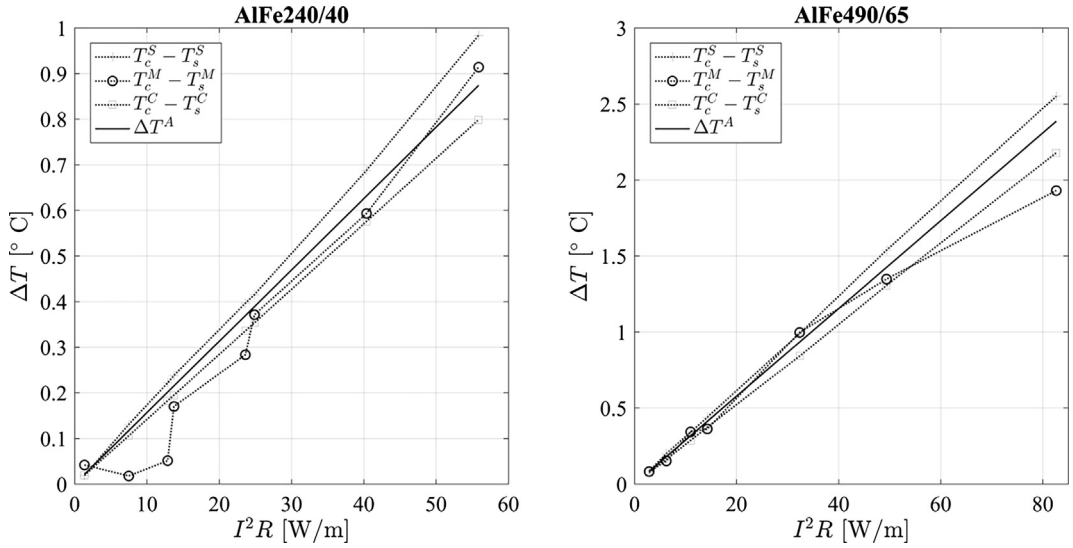

Fig. 16. Skin-core difference as a function of the joule losses.

80 °C at 1000 A, as shown in Fig. 12. This means that forced convection cooling at 0.6 m/s wind is noticeably larger than cooling due to the natural convection.

In all above discussions we assumed that the thermal conductivity of the conductors is known. Thermal conductivity of aluminium is known to be approximately $\lambda_{Al} = 200$ W/mK, nevertheless, the majority of the radial thermal transfer occurs through the air pockets between the individual conductor strands [22]. In addition, the contact between the strands is not ideal; the pressure on the contacts between the conductor strands is variable and heavily depends on the tension put on the conductor that is created by hanging it from poles. Thus the effective radial thermal conductivity of the conductor is in the order of $\lambda \in [0.5, 7]$ W/mK [11]. Using simple heat transfer model [22] we can estimate difference between surface and core temperature as

$$\Delta T^A = T_c - T_s = \frac{I^2R}{2\lambda\pi}\left[\frac{1}{2} - \frac{D_1^2}{D^2 - D_1^2}\ln\left(\frac{D}{D_1}\right)\right], \tag{23}$$

where D and D_1 are conductor diameter and steel core diameter, and T_c core temperature. As can be seen from this simple model, the only free parameter that has an effect on the temperature difference between the conductor core and surface is the heat conductivity. Therefore this parameter can be extracted from the measurements made in the steady state. To do this, we use the same segmentation as in Section 4. In all measured steady-states a difference between skin and core temperature (ΔT) is expressed as a function of Joule losses, from which we get estimated values $\lambda = 2$ W/mK for Al/Fe 490/65 and $\lambda = 3.5$ W/mK for Al/Fe 240/40. Graphs of ΔT^A as a function of Joule losses are plotted in Fig. 16, where λ is calculated as the coefficient of the approximated linear function.

6. Conclusions

This paper evaluates the cooling of overhead conductors of the power lines due to the natural convection. First, confidence in numerical assessment of conductor temperature is established by achieving good agreement when comparing two conceptually different numerical approaches and the experimentally gathered data. The validity of algorithms found in CIGRE and IEEE guidelines is tested by comparing them with results obtained by a proposed thermo-fluid simulation and with measured temperatures in a controlled experimental environment for two different conductors. The comparison shows that the differences between the performed simulation, existing guidelines and the experimentally obtained results are below 2% for Al/Fe 240/40 conductor and mostly below 3% for Al/Fe 490/65 conductor. There is also no significant difference between CIGRE and IEEE predictions, while IEC does not consider cooling due to the natural convection.

With a validated solution procedure we have shown that the forced convection cooling at 0.6 m/s wind is noticeably larger than cooling

due to the natural convection at conditions considered in EN 50182.

In the future we will continue with measurements to clarify open issues, e.g. discrepancy in cooling dynamics. From the modelling point of view an appropriate weathering model to predict emissivity is required. The numerical simulation will be improved with stabilization of advection term in Navier-Stokes equation in order to compute the forced convection.

Acknowledgment

The authors would like to acknowledge the financial support of ELES, Ltd., Slovenian Electricity Transmission System Operator, and Slovenian Research Agency (ARRS) in the framework of the research core funding No. P2-0095.

Appendix A. Supplementary material

Supplementary data to this article can be found online at https://doi.org/10.1016/j.ijepes.2019.05.005.

References

[1] UCTE System disturbance on 4 November 2006, Final report. UCTE; 2007.
[2] UCTE. FINAL REPORT of the investigation committee on the 28 September 2003 Blackout in Italy; 2004.
[3] Berizzi A. The Italian 2003 blackout. IEEE power engineering society general meeting, vol. 2; 2004. p. 1673–9.
[4] Kosec G, Maksić M, Djurica V. Dynamic thermal rating of power lines – model and measurements in rainy conditions. Int J Electr Power Energy Syst 2017;91:222–9. https://doi.org/10.1016/j.ijepes.2017.04.001.
[5] Piccolo A, Vaccaro A, Villacci D. Thermal rating assessment of overhead lines by Affine Arithmetic. Electr Power Syst Res 2004;71:275–83. https://doi.org/10.1016/j.epsr.2004.01.018.
[6] Zhan J, Chung CY, Demeter E. Time series modeling for dynamic thermal rating of overhead lines. IEEE Trans Power Syst 2017;32:2172–82. https://doi.org/10.1109/TPWRS.2016.2596285.
[7] Pytlak P, Musilek P, Lozowski E, Toth J. Modelling precipitation cooling of overhead conductors. Electr Power Syst Res 2011;81:2147–54.
[8] Morgan VT. The thermal rating of overhead-line conductors. Electr Power Syst Res 1981;5:119–39.
[9] Karimi S, Musilek P, Knight AM. Dynamic thermal rating of transmission lines: a review. Renew Sustain Energy Rev 2018;91:600–12. https://doi.org/10.1016/j.rser.2018.04.001.
[10] Michiorri A, Nguyen H-M, Alessandrini S, Bremnes JB, Dierer S, Ferrero E, et al. Forecasting for dynamic line rating. Renew Sustain Energy Rev 2015;52:1713–30. https://doi.org/10.1016/j.rser.2015.07.134.
[11] CIGRE. Guide for thermal rating calculations of overhead lines. CIGRE; 2014.
[12] IEEE standard for calculating the current-temperature relationship of bare overhead conductors. IEEE Std.; 2014. p. 738–2012.
[13] Commission IE. Technical committee 20—overhead electrical conductors. International Electrotechnical Commission; 2016.
[14] Arroyo A, Castro P, Martinez R, Manana M, Madrazo A, Lecuna R, et al. Comparison between IEEE and CIGRE thermal behaviour standards and measured temperature on a 132-kV overhead power line. Energies 2015;8:13660–71. https://doi.org/10.3390/en81212391.
[15] House HE, Tuttle PD. Current-carrying capacity of acsr. AIEE transactions on power apparatus and systems. 1958. p. 1169–78.
[16] McAdams WH. Heat transmission. McGraw-Hill Inc.; 1954.
[17] Morgan V. The overall convective heat transfer from smooth circular cylinders. Adv Heat Transf 1975;1:199–264.
[18] Zhukauskas A, Žiugžda J. Heat transfer of a cylinder in crossflow. Hemisphere Pub.; 1985.
[19] Natural convection, Special course report. Electronic power engineering, Orsted, DTU Technical University of Denmark; 2005.
[20] Kosec G, Slak J. RBR-FD based dynamic thermal rating of overhead power lines. Twelfth international conference on advances in fluid mechanics. Ljubljana: WIT Press; 2018.
[21] Medusa: coordinate free meshless method implementation. http://e6.ijs.si/medusa/.
[22] Morgan VT. The radial temperature distribution and effective radial thermal conductivity in bare solid and stranded conductors. IEEE Trans Power Deliv 1990;5:1443–52.
[23] Schurig OR, Frick CW. Heating and current-carrying capacity of conductors for outdoor service. Gen Electr Rev 1930;33:141–57.
[24] EN 50182:2002 conductors for overhead lines. Round wire concentric lay stranded conductors; 2002.